

# Dual imaging modality of fluorescence and transmission X-rays for gold nanoparticle-injected living mice

Taeyun Kim<sup>1</sup>  | Woo Seung Lee<sup>1</sup> | Miyeon Jeon<sup>1</sup> | Hyejin Kim<sup>1</sup> | Mingi Eom<sup>1</sup> | Seongmoon Jung<sup>2</sup>  | Hyung-Jun Im<sup>1,3</sup>  | Sung-Joon Ye<sup>1,3,4,5</sup> 

<sup>1</sup>Department of Applied Bioengineering, Graduate School of Convergence Science and Technology, Seoul National University, Seoul, South Korea

<sup>2</sup>Department of Radiation Oncology, Seoul National University Hospital, Seoul, South Korea

<sup>3</sup>Research Institute for Convergence Science, Seoul National University, Seoul, South Korea

<sup>4</sup>Advanced Institute of Convergence Technology, Seoul National University, Suwon, South Korea

<sup>5</sup>Biomedical Research Institute, Seoul National University Hospital, Seoul, South Korea

## Correspondence

Sung-Joon Ye, Department of Applied Bioengineering, Graduate School of Convergence Science and Technology, Seoul National University, Seoul 08826, South Korea. Email: [syje@snu.ac.kr](mailto:syje@snu.ac.kr)

## Funding information

Korea government (MSIT), Grant/Award Number: 1711078081; Korea Foundation Of Nuclear Safety (KoFONS); Nuclear Safety and Security Commission (NSSC) of the Republic of Korea, Grant/Award Number: 2003021

## Abstract

**Background:** X-ray fluorescence (XRF) imaging for metal nanoparticles (MNPs) is a promising molecular imaging modality that can determine dynamic biodistributions of MNPs. However, it has the limitation that it only provides functional information.

**Purpose:** In this study, we aim to show the feasibility of acquiring functional and anatomic information on the same platform by demonstrating a dual imaging modality of pinhole XRF and computed tomography (CT) for gold nanoparticle (GNP)-injected living mice.

**Methods:** By installing a transmission CT detector in an existing pinhole XRF imaging system using a two-dimensional (2D) cadmium zinc telluride (CZT) gamma camera, XRF and CT images were acquired on the same platform. Due to the optimal X-ray spectra for XRF and CT image acquisition being different, XRF and CT imaging were performed by 140 and 50 kV X-rays, respectively. An amount of 40 mg GNPs (1.9 nm in diameter) suspended in 0.20 ml of phosphate-buffered saline were injected into the three BALB/c mice via a tail vein. Then, the kidney and tumor slices of mice were scanned at specific time points within 60 min to acquire time-lapse in vivo biodistributions of GNPs. XRF images were directly acquired without image reconstruction using a pinhole collimator and a 2D CZT gamma camera. Subsequently, CT images were acquired by performing CT scans. In order to confirm the validity of the functional information provided by the XRF image, the CT image was fused with the XRF image. After the XRF and CT scan, the mice were euthanized, and major organs (kidneys, tumor, liver, and spleen) were extracted. The ex vivo GNP concentrations of the extracted organs were measured by inductively coupled plasma mass spectrometry (ICP-MS) and L-shell XRF detection system using a silicon drift detector, then compared with the in vivo GNP concentrations measured by the pinhole XRF imaging system.

**Results:** Time-lapse XRF images were directly acquired without rotation and translation of imaging objects within an acquisition time of 2 min per slice. Due to the short image acquisition time, the time-lapse in vivo biodistribution of GNPs was acquired in the organs of the mice. CT images were fused with the XRF images and successfully confirmed the validity of the XRF images. The difference in ex vivo GNP concentrations measured by the L-shell XRF detection system and ICP-MS was 0.0005–0.02% by the weight of gold (wt%). Notably, the in vivo and ex vivo GNP concentrations in the kidneys of three mice were comparable with a difference of 0.01–0.08 wt%.

**Conclusions:** A dual imaging modality of pinhole XRF and CT imaging system and L-shell XRF detection system were successfully developed. The developed systems are a promising modality for in vivo imaging and ex vivo

quantification for preclinical studies using MNPs. In addition, we discussed further improvements for the routine preclinical applications of the systems.

#### KEYWORDS

computed tomography, dual imaging modality, gold nanoparticles, in vivo molecular imaging, X-ray fluorescence imaging

## 1 | INTRODUCTION

Metal nanoparticles (MNPs) have been emerging nanomedicine materials for drug delivery and as radiosensitizers, owing to their unique properties.<sup>1</sup> Among various candidate MNPs of high atomic number ( $Z$ ) (e.g., gadolinium, platinum, silver, hafnium, and gold), gold nanoparticles (GNPs) are particularly promising.<sup>2–4</sup> As an inert metal, GNPs have better biocompatibility and less toxicity than other MNPs. Moreover, GNPs can be synthesized in various sizes and shapes depending on the characteristics of the target tumor, and surface modification can be applied to improve their tumor targeting ability.<sup>5,6</sup>

Prior to preclinical and clinical applications of GNPs, determining the ex vivo and in vivo biodistribution of GNPs is crucial. Inductively coupled plasma–mass spectrometry (ICP–MS) and inductively coupled plasma–atomic emission spectroscopy have been used for ex vivo quantification of GNP concentrations.<sup>7,8</sup> These methods have the advantage of a very low detection limit (i.e., in ppt–ppb) and a high degree of reliability, but a complex sample preparation process is essential (e.g., lyophilized, dissolved, and diluted). Optical fluorescence imaging and photoacoustic imaging have been used to determine the in vivo biodistribution of GNPs.<sup>9,10</sup> However, optical-based molecular imaging modalities have the disadvantage of the limited penetration depth to a few mm depending on an imaging signal.<sup>11</sup>

X-ray fluorescence (XRF) imaging and X-ray fluorescence computed tomography (XFCT) using GNP as a contrast agent are promising molecular imaging modalities that are based on XRF photons.<sup>7,12–16</sup> XRF photon-based imaging modalities with a benchtop system and a polychromatic X-ray source have been widely investigated in preclinical studies because of the ease of implementation in the laboratory scale. These molecular imaging modalities are superior to optical-based molecular imaging modalities in terms of penetration depth because they use high-energy XRF photons (e.g., gold  $K_{\alpha 1}$  and  $K_{\alpha 2}$  at 68.8 and 67.0 keV, respectively) as an imaging signal. However, the aforementioned molecular imaging modalities have the common drawback of providing only functional information. This drawback can be solved by combining with an imaging modality, such as computed tomography (CT), which provides anatomic information.<sup>17</sup>

In 2020, a benchtop XFCT study with a linear array cadmium zinc telluride (CZT) detector and a single pinhole collimator was reported for in vivo imaging of NaGdF<sub>4</sub> NPs.<sup>18</sup> Fused images of XFCT and CT confirmed the feasibility of NaGdF<sub>4</sub> as a contrast agent for the liver and lungs of mice. However, the validity of the fused images might be questioned because the XFCT and CT images were acquired from different experimental setups. More recently, a benchtop XFCT system was developed for in vivo longitudinal imaging of molybdenum oxide (MoO<sub>2</sub>) NPs in mice.<sup>19</sup> XFCT and CT images were simultaneously acquired using a custom three-element silicon drift detector (SDD) and a transmission detector. A short image acquisition time of 1.5 min per slice and a spatial resolution of a few-100  $\mu\text{m}$  were demonstrated. However, the low-energy XRF photon of MoO<sub>2</sub> NPs ( $K_{\alpha 1}$  at 17.4 keV) might not be suitable for thick imaging objects. In 2021, multiplexed in situ XFCT imaging of MoO<sub>2</sub>, rhodium, and ruthenium NPs was performed using this benchtop XFCT system.<sup>20</sup>

In this paper, by installing a flat panel detector (FPD) on an existing pinhole XRF imaging system, we investigated the feasibility of a dual imaging modality for dynamic in vivo XRF images and CT images. The optimal energy spectra of XRF and CT imaging were different; as a result, the XRF and CT images were sequentially acquired on the same platform. In addition, time-lapse in vivo biodistributions of GNPs in the three BALB/c mice were acquired to determine the response of organs to the administration of 1.9 nm GNPs without surface modification. Moreover, a pre-developed L-shell XRF detection system was cross-validated with the other modalities (ICP–MS and pinhole XRF system). The in vivo and ex vivo GNP concentrations measured by the pinhole XRF images and the L-shell XRF detection, respectively, were compared and validated by ICP–MS.

## 2 | METHODS AND MATERIALS

### 2.1 | Pinhole X-ray fluorescence and computed tomography imaging system

Figure 1a shows the dual modality pinhole XRF and CT imaging system, which was developed by installing a transmission CT detector (complementary metal–oxide–semiconductor FPD (Dexela 1207, PerkinElmer,

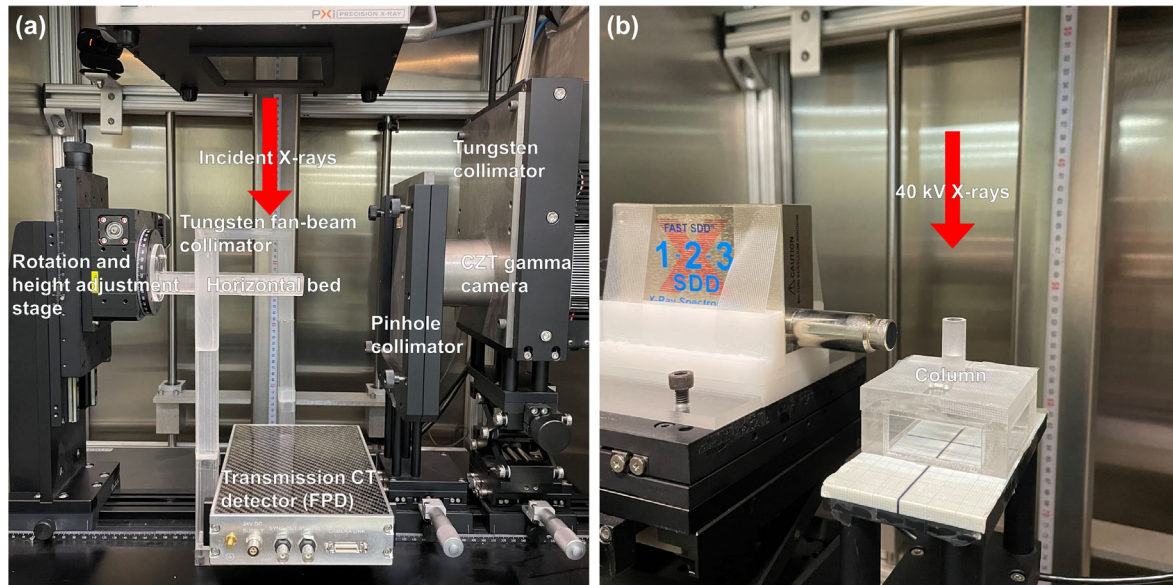


**FIGURE 1** (a) Photograph of the dual modality pinhole X-ray fluorescence (XRF) and computed tomography (CT) imaging system. Imaging objects (i.e., polymethyl methacrylate [PMMA] phantom and mice) were placed on the horizontal bed. (b) Photograph of the L-shell XRF detection system. The column was filled with gold nanoparticle (GNP)-containing solutions or extracted organs of mice.

Waltham, MA, USA)) in an existing pinhole XRF imaging system. The FPD comprised  $1536 \times 864$  transistors and photodiodes (i.e., pixel). It had a pixel pitch of  $74.8 \mu\text{m}$  and an active area of  $114.9 \text{ mm} \times 64.6 \text{ mm}$ . Cesium iodide (CsI) was used as a scintillator. A carbon fiber window was positioned in front of the CsI scintillator to shield ambient light and to provide mechanical protection. The FPD was used to detect transmitted X-rays through the imaged objects. In order to minimize the interference with transmitted X-rays, a custom-made horizontal bed was created to minimize the effect of the surrounding material. The distance between the imaged objects and the FPD was made as close as possible using a rotation and height adjustment stage to minimize geometric penumbra. The source-to-object distance and the object-to-detector distance were 60 and 7 cm, respectively. Dark current, gain, and defective pixel corrections were carried out according to the manufacturer's instructions.

The pinhole XRF imaging system comprised a tungsten fan beam collimator, a horizontal bed, a lead pinhole collimator, a tungsten collimator, and a CZT gamma camera (Integrated Detector Electronics AS, Oslo, Norway). The tungsten fan beam collimator was used for X-rays that interacted with the GNP-injected objects to generate K-shell XRF photons and Compton-scattered photons. These secondary photons were detected by the CZT gamma camera through the lead pinhole collimator. The field of view (FOV) of the CZT gamma camera was  $5.12 \text{ cm} \times 5.12 \text{ cm}$  and comprised  $32 \times 32$  pixels with a  $1.6 \text{ mm}$  pixel pitch. According to the theoretical equation for spatial resolution of the pinhole imaging system,<sup>21</sup> the spatial resolution of our pin-

hole XRF imaging system was  $4.4 \text{ mm}$ . In order to minimize unwanted photons caused by incident X-rays, the pinhole collimator and the CZT gamma camera were placed perpendicular to the direction of incident X-rays, and the tungsten collimator was attached to the front Al window of the CZT gamma camera. The detailed specifications and characteristics of the pinhole XRF imaging system were described in our early study.<sup>7</sup>

A small animal-sized phantom ( $2.5 \text{ cm}$  in diameter,  $5 \text{ cm}$  in length) that was made of polymethyl methacrylate (PMMA) was used to obtain a calibration curve to correlate GNP concentrations with the K-shell XRF photon counts. In the PMMA phantom center, a column of  $0.64 \text{ cm}$  in diameter and  $1 \text{ cm}$  in height was inserted and was filled with GNP-containing solutions. GNPs of  $1.9 \text{ nm}$  in diameter (AuroVist, Nanoprobe Inc., Yaphank, NY, USA) were prepared according to the manufacturer's instructions and were serially diluted with deionized water. The concentrations of the GNP-containing solutions ranged from  $0.125\text{--}2.0\%$  by the weight of gold, or wt% ( $1.25\text{--}20 \text{ mg/ml}$ ). The PMMA phantom was scanned for 1 min to obtain the K-shell XRF photon counts for each GNP concentration; this measurement was repeated 10 times. For detection limit analysis, the contrast-to-noise ratio (CNR) was calculated as follows:

$$\text{CNR} = (\overline{\text{XRF}}_{\text{ROI}} - \overline{\text{Bg}}) / \sigma_{\text{Bg}} \quad (1)$$

where  $\overline{\text{XRF}}_{\text{ROI}}$  and  $\overline{\text{Bg}}$  were the average photon counts in the region of interest (ROI) and in the background

region of the raw XRF image, respectively. The ROI was defined as  $4 \times 6$  pixels ( $0.64 \text{ cm} \times 0.96 \text{ cm}$ ) and was the region projected by the GNP-filled column. The background region was defined as that which had the same dimension as the ROI (i.e.,  $4 \times 6$  pixels) and was two pixels away from the ROI in the  $y$ -direction.  $\sigma_{\text{BG}}$  value was the standard deviation of the average photon counts in the background region.

## 2.2 | L-shell X-ray fluorescence detection system

Figure 1b shows the L-shell XRF detection system with an SDD (X-123SDD, Amptek Inc., Bedford, MA, USA). X-rays of 40 kV filtered with 2 mm Al were used to stimulate GNPs. The X-ray tube current was 10 mA. Two dominant gold L-shell XRF peaks ( $L_{\alpha 1}$  and  $L_{\beta 1}$  at 9.71 and 11.4 keV, respectively) were used to measure the L-shell XRF photon counts. The same column (0.64 cm in diameter, 1 cm in height) used in the pinhole XRF imaging system was scanned without a PMMA phantom. The distance between the detector head and the column center was 3 cm. The calibration curve between the GNP concentrations and the L-shell XRF photon counts was obtained using GNP-containing solutions ranging from 0.0078–1.0 wt% (0.078–10 mg/ml). The scan time was 5 min for each GNP concentration, and measurement was repeated three times.

## 2.3 | X-ray sources and radiation dose

Polychromatic X-rays were generated using an X-RAD 320 biological irradiator (Precision X-Ray Inc., North Branford, CT, USA) with a tungsten target. In order to generate K-shell XRF photons of GNPs, the incident X-ray energy must be above the 80.7 keV gold K-edge energy. Thus, pinhole XRF imaging was performed using a fan beam of 140 kV X-rays filtered with 1.5 mm Al, 0.25 mm Cu, and 0.75 mm Sn. However, because these high-energy X-rays do not produce sufficient contrast on CT, a cone beam of 50 kV X-rays filtered with 0.5 mm Al was used for the CT scan. The X-ray tube currents were 18 mA for XRF imaging and 10 mA for CT scan. The half-value layers of XRF and CT X-ray sources were 14.6 mm Al and 0.60 mm Al, respectively. Their mean energy was 97.6 and 26.2 keV, respectively, in which SpekCalc software was used to calculate.

The radiation doses to the skin of mice during XRF imaging and CT scan were measured by thermoluminescent dosimeters (TLDs) (Harshaw TLD-100, Thermo Fisher Scientific Inc., Waltham, MA, USA). TLDs were divided into two groups, which were calibrated by filtered 140 and 50 kV X-rays, respectively. The reference dosimetry was performed by following the AAPM

TG-61 protocol using a PTW 30013 Farmer-type ionization chamber (PTW-Freiburg, Freiburg, Germany). The luminescent signals of the TLDs were read by a Harshaw 3500 TLD reader (Thermo Fisher Scientific Inc., Waltham, MA, USA).

## 2.4 | Mice study

Three 6-week-old female BALB/c mice bearing the subcutaneous 4T1 breast tumor were used (IACUC2004-022, Nov. 09, 2020). Mice were obtained from Orient Bio (322 Galmachi-ro, Jungwon-gu, Seongnam-si, Gyeonggi-do, Korea), and care and management were conducted at Woojung Bio (593-8 Dongtan-ro, Hwasung-si, Gyeonggi-do, Korea), maintaining a normal state in a specific pathogen-free area. The tumor was allowed to grow to about  $200 \text{ mm}^3$  for 14 days from the time of cancer cells inoculation. Mice experiments were performed after confirming no abnormal changes such as weight loss during tumor growth. The mice were restrained on the horizontal bed and anesthetized with isoflurane gas via inhalation for 70 min without recovery. The kidney and tumor locations were marked on the surface of the mice, and those were scanned for 1 min before the injection of the GNP-containing solution (i.e., preinjection scanning). The slice thickness was 2 mm. Subsequently, 40 mg of GNPs (1.9 nm in diameter) suspended in 0.20 ml of phosphate-buffered saline was injected through the tail vein. This was the same dose of 1.9 nm GNPs as in our early study<sup>7</sup> to generate a biodistribution that would allow comparison with the previous results.<sup>16</sup> Then, the kidney and tumor slices were scanned (i.e., postinjection scanning) for 1 min at specific time points, as follows:  $T = 0$  (i.e., immediately after the injection) and at 10, 20, 40, and 60 min. The time-lapse XRF images of the kidney and tumor slices were separately acquired using the direct subtraction method, which was described in Section 2.5.

After the XRF imaging at  $T = 60$  min, a CT scan was sequentially performed by adjusting the distance between the horizontal bed and the FPD and removing the tungsten fan beam collimator. After the CT scan, the mice were euthanized via  $\text{CO}_2$  inhalation. The major organs were extracted and subjected to measurement by an L-shell XRF detection system without a sample preparation process. Subsequently, in ICP-MS system (Nexion 350D, PerkinElmer, Waltham, MA, USA), extracted organs were lyophilized and digested sequentially with 8 ml of  $\text{HNO}_3$  and 8 ml of aqua regia (2 ml of  $\text{HNO}_3$ , 6 ml of HCl). The digestion process was conducted on a hot plate at  $160^\circ\text{C}$  for 3 h. Ex vivo GNP concentrations were measured as the average of triplicate measurements. All animal experiments were performed in accordance with the guidelines approved by the Institutional Animal Care and Use Committee in Woojung BIO.

## 2.5 | Data acquisition and image processing

Two gold  $K_{\alpha}$  XRF peaks (68.8 and 67.0 keV) were used to measure the K-shell XRF photon counts. However, because of the intrinsic limitation on energy resolution (11.1 keV full width at half maximum at 59.5 keV) of the CZT gamma camera, peaks were overlapped as a single peak between 65.6 and 71.0 keV; this peak was used to acquire an XRF image. The raw XRF photon counts of each pixel were obtained using the direct subtraction method, in which the photon counts of the imaged objects without GNPs (i.e., Compton-scattered photon counts) were subtracted from that of the imaged objects with GNPs (i.e., XRF and Compton-scattered photon counts) to eliminate Compton background. The corrected XRF photon counts were obtained by multiplying the attenuation, sensitivity, and pixel-by-pixel nonuniformity correction factors by the raw XRF photon counts; a detailed explanation about correction factors can be found in our previous studies.<sup>7,15</sup> The corrected values were converted into the GNP concentrations using a calibration curve. A two-dimensional (2D) map of the GNP concentrations with  $32 \times 32$  pixels (i.e., raw XRF image) was acquired and smoothed as  $512 \times 512$  pixels by applying bicubic interpolation. The XRF image acquisition process was implemented in MATLAB (R2020a, MathWorks Inc., Natick, MA, USA).

For the CT scan, the imaged objects were scanned for 3 s per projection, including exposure time (47 ms), detector readout, and stage rotation. The rotation stage rotated an imaged object, with a  $2^{\circ}$  increment using the manufacturer-provided software to acquire 180 projections (i.e.,  $360^{\circ}$  rotation). A ring artifact correction algorithm was applied to reduce the ring artifact caused by the nonuniformity of the sensitivity of the FPD elements.<sup>22</sup> CT images were reconstructed using a filtered back projection algorithm. Image reconstruction was implemented using Scikit-Image, which is an open-source image processing library in Python. The FOV of CT images was 5.1 cm and consisted of  $470 \times 470$  voxels with a size of  $108.5 \mu\text{m}$ . The CT image acquisition took about 10 min. In order to fuse XRF and CT images, we relied on the dorsal structure of the mouse. Because the position of the mouse was kept the same under anesthesia during the XRF and CT imaging, we postulated that it could be possible to determine the relative position of the mouse using the dorsal structure of the mouse, which was well distinguished in both XRF and CT images. The spatial resolution of the CT imaging system was estimated using the modulation transfer function (MTF).<sup>23,24</sup> The edge spread function (ESF) was determined from the CT image of a small animal-sized phantom, and then MTF was obtained by taking the Fourier transform of the first derivative of ESF. In addition, CNR was calculated in the same ROI to evaluate the quality and detectability of the CT image.

The average Hounsfield units were used instead of the average photon counts of the ROI and background.

## 3 | RESULTS

### 3.1 | Calibration curves

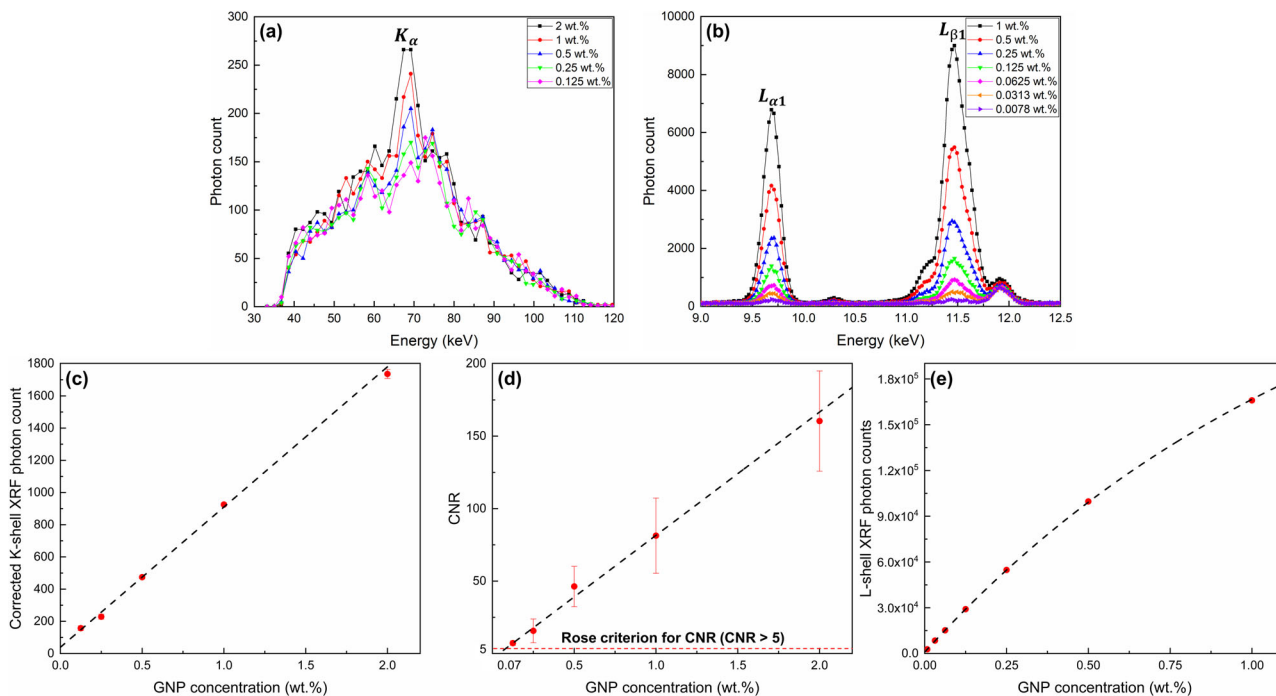
Figure 2a,b shows the K-shell and L-shell XRF spectra measured with different concentrations of GNP-containing solutions to obtain calibration curves. Figure 2c shows the calibration curve of the pinhole XRF imaging system obtained from the PMMA phantom. The black dashed line in the linear regression curve indicated a good linear relationship (i.e.,  $R^2 = 0.9989$ ) between the GNP concentrations and the corrected K-shell XRF photon counts. According to the Rose criterion for CNR ( $\text{CNR} > 5$ ),<sup>21</sup> the lowest detectable concentration of GNPs in the XRF images was about 0.07 wt% (Figure 2d).

Figure 2e shows the calibration curve of the L-shell XRF detection system obtained from the column. The L-shell XRF photons were self-absorbed in the samples because of their lower energy and higher attenuation by the GNP-filled column. In particular, L-shell XRF photons were self-absorbed more at higher concentrations of GNP-filled column. As a result, an exponential relationship (i.e.,  $R^2 = 0.9999$ ) was obtained between the GNP concentrations and the L-shell XRF photon counts.

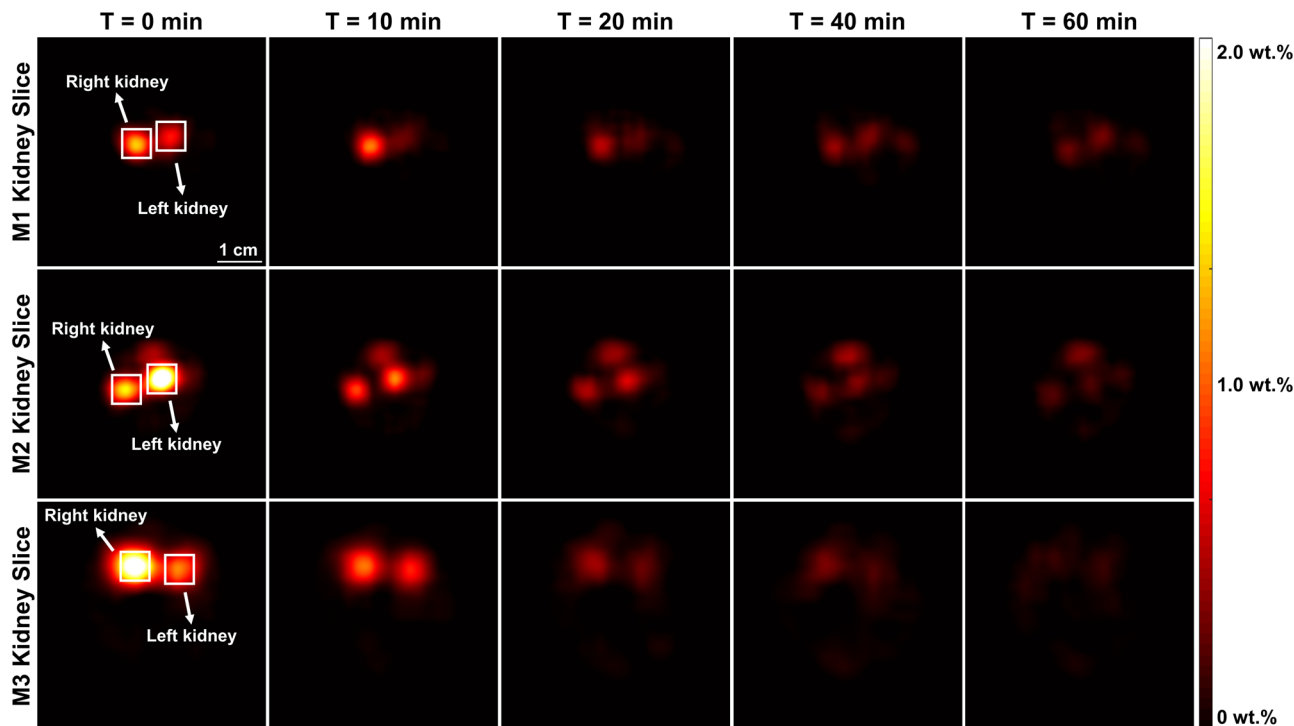
### 3.2 | Pinhole X-ray fluorescence and computed tomography imaging system

Figure 3 shows the time-lapse XRF images of kidney slices from mouse 1 (M1), mouse 2 (M2), and mouse 3 (M3). Figure 4 shows the CT image fused with the time-lapse XRF images of a kidney slice from M3 and the CT image fused with the time-lapse XRF images of a tumor slice from M1. The left and right kidneys of the three mice were clearly identified on the XRF images. The difference in GNP concentrations of the left and right kidneys was expected to be due to the mouse-to-mouse variation of the anatomical location of the kidneys and biological response (e.g., kidney clearance of GNPs and biodistribution of GNPs in the kidneys<sup>26</sup>).

On the other hand, XRF images of the tumor slice were not observed; we speculated that this was because the amount of GNPs in the tumor was below the detection limit of the pinhole XRF imaging system. However, the time-lapse XRF images of the bladder from M1 were acquired and fused with the CT images that identified the tumor and bladder. The kidneys and bladder regions that were seen on both the XRF and CT images were well matched in the fusion image. CT/XRF fusion images succeeded in adding anatomic information, which the XRF images alone could not provide.



**FIGURE 2** (a) K-shell X-ray fluorescence (XRF) spectra measured by the cadmium zinc telluride (CZT) gamma camera. (b) L-shell XRF spectra measured by the silicon drift detector (SDD). (c) Linear relationship between gold nanoparticle (GNP) concentrations and corrected K-shell XRF photon counts. (d) Contrast-to-noise ratio (CNR) of the XRF image for each GNP concentration. (e) Exponential relationship between GNP concentrations and L-shell XRF photon counts. Error bars indicate a 95% confidence interval of the mean. The sizes of error bars and data symbols in (c) and (e) are similar.



**FIGURE 3** The first row is the time-lapse X-ray fluorescence (XRF) images of the kidneys of M1, the second row is the time-lapse XRF images of the kidneys of M2, and the third row is the time-lapse XRF images of the kidneys of M3. The white boxes in the first column indicate the region for average gold nanoparticle (GNP) concentrations quantification.

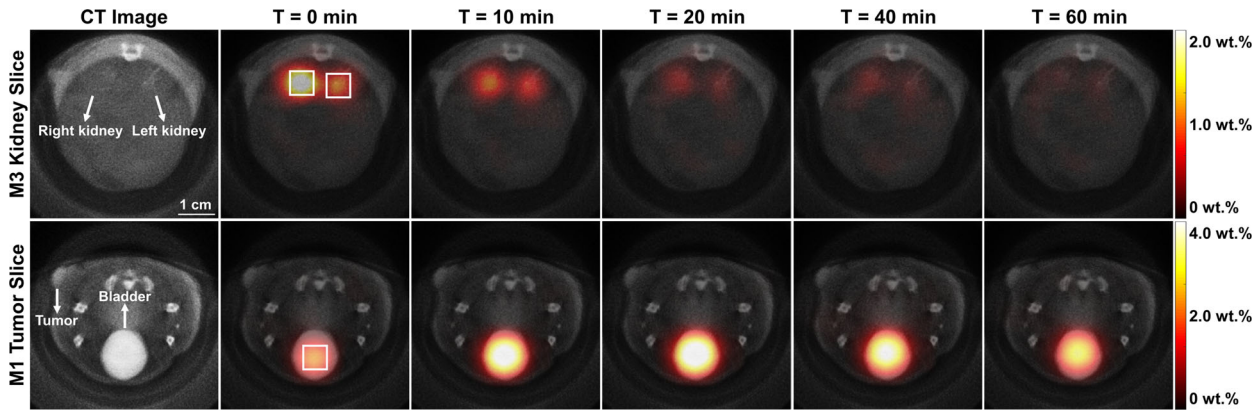


**FIGURE 4** The first row is the computed tomography (CT) image, time-lapse X-ray fluorescence (XRF) images fused with the CT image of a kidney slice from M3, and the second row is the CT image, time-lapse XRF images fused with the CT image of a tumor slice from M1. The white boxes in the second column indicate the region for average gold nanoparticle (GNP) concentrations quantification.

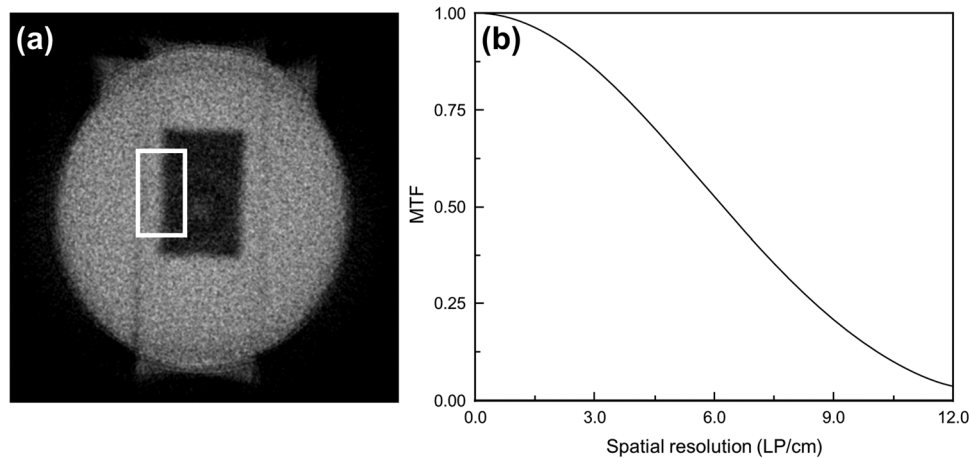


**FIGURE 5** (a) Computed tomography (CT) image of small animal-sized phantom. The white box indicates the edge region used for modulation transfer function (MTF) calculation. (b) Corresponding MTF curve at the white box in (a)

**TABLE 1** Contrast-to-noise ratios (CNRs) on X-ray fluorescence (XRF) ( $T = 0$  min) and computed tomography (CT) images for kidneys of M3 and bladder of M1

Organ	CNR	
	XRF image	CT image
Left kidney	32.6	0.83
Right kidney	60.3	1.33
Bladder	39.5	14.8

However, motion artifacts due to gravity were inevitable because the mouse was rotated while being restrained on a horizontal bed. Figure 5 shows the CT image of a small animal-sized phantom and the corresponding MTF curve. The MTF curve demonstrates a spatial resolution of 6.2 line pairs per centimeter (LP/cm) at 50% MTF. Table 1 summarizes CNRs on the XRF and CT images. The kidneys and bladder were detectable in XRF images (i.e.,  $CNR > 5$ ). However, only the bladder

was detectable in CT images in this criteria. This result highlights the importance of XRF images to accurately determine the in vivo biodistribution of GNPs. The radiation doses measured with TLDs during the XRF imaging were 59.1 mGy per slice (i.e., the sum of the pre- and the postinjection scanning) and 354 mGy per mouse (i.e., total radiation dose for XRF imaging). The radiation dose of the CT scan was 321.7 mGy.

The GNP clearance curves in the kidneys and the GNP accumulation curve in the bladder are shown in Figure 6a,b, respectively. In order to quantify the average GNP concentrations in the raw XRF images,  $4 \times 4$  pixels in the kidneys and bladder region were used. The error bars indicated a 95% confidence interval of  $4 \times 4$  mean pixel values. The GNP concentrations in the kidneys of three mice were maximum at  $T = 0$  min and were rapidly excreted. On the other hand, the GNPs excreted from the kidneys accumulated in the bladder. The minimum and maximum GNP concentrations in the bladder of M1 were at  $T = 0$  and 20 min, respectively. Thereafter,

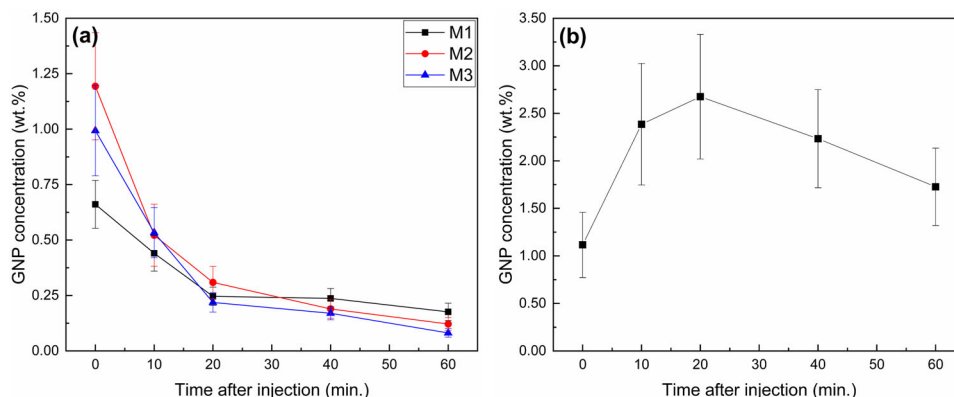


**FIGURE 6** (a) Gold nanoparticle (GNP) clearance curves in the kidneys of M1, M2, and M3. At  $T = 0$  min, the GNP concentrations of the kidneys differ among the mice but show a similar excretion rate over 10–60 min. (b) GNP accumulation curve in the bladder of M1. Because the GNPs excreted from the kidneys accumulate in the bladder, they show an opposite tendency to the GNPs clearance curve in the kidneys.

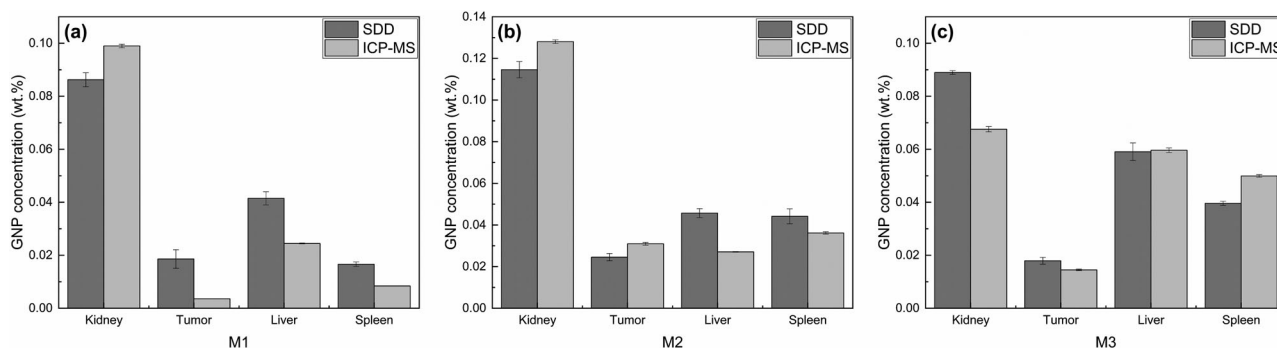


**FIGURE 7** Ex vivo gold nanoparticle (GNP) concentrations of the extracted organs from (a) M1, (b) M2, and (c) M3 are measured by the L-shell X-ray fluorescence (XRF) detection system (silicon drift detector [SDD]) and inductively coupled plasma mass spectrometry (ICP-MS). Error bars indicate a 95% confidence interval of the mean

the GNPs were gradually diluted by the metabolism of mice.

### 3.3 | L-shell X-ray fluorescence detection system

The ex vivo GNP concentrations of the extracted organs from the three mice were measured and compared by the L-shell XRF detection system and ICP-MS (Figure 7). The difference in the measured ex vivo GNP concentrations between the L-shell XRF detection system and ICP-MS was 0.0005–0.02 wt%. The lowest detectable GNP concentration using the L-shell XRF detection system was about 0.02 wt%. The GNP concentration of the tumor was up to  $0.026 \pm 0.007$  wt%, which was lower than the detection limit of the pinhole XRF imaging system; thus, XRF images of the tumor slice could not be acquired. The in vivo and ex vivo GNP concentrations in the kidneys measured by the pinhole XRF imaging system (M1:  $0.17 \pm 0.03$  wt%, M2:  $0.12 \pm 0.02$  wt%, M3:  $0.08 \pm 0.01$  wt%) and the L-shell XRF detection system (M1:  $0.086 \pm 0.003$  wt%, M2:  $0.115 \pm 0.004$  wt%, M3:  $0.0889 \pm 0.0006$  wt%)

were comparable. Furthermore, those were successfully validated by ICP-MS (M1:  $0.0990 \pm 0.0006$  wt%, M2:  $0.1281 \pm 0.0008$  wt%, M3:  $0.0676 \pm 0.0009$  wt%).

## 4 | DISCUSSION

A dual modality of pinhole XRF and CT imaging system was developed by adding a transmission detector to the existing pinhole XRF imaging system. The pinhole XRF imaging system, which can directly acquire 2D XRF images without image reconstruction due to pinhole collimator and a 2D CZT gamma camera, could acquire time-lapse XRF images from the kidneys and bladder of living mice. In addition, it is important to note that unlike the other dual imaging modalities of XRF and CT using single-crystal or linear array detectors,<sup>8,18–20</sup> a 2D array detector used in this study can address the key technical limitations of single-crystal or linear array detectors. The use of a 2D array detector has been proved to reduce the excessive image acquisition time and radiation dose during XRF imaging. Until now, XRF studies using 2D array detectors have rarely been reported.<sup>7,37,38</sup> However, with the energy and spatial resolutions of 2D array



detectors improved, those will be widely used in XRF imaging. Hence, a dual imaging modality of pinhole XRF and CT demonstrated will provide useful information for the implementation of dual imaging modality XRF and CT systems using 2D array detectors.

The 1.9 nm in diameter GNPs were accumulated in the kidneys immediately after injection and were rapidly excreted into the urine over time. In this study, time-lapse XRF images of both kidneys from three mice were successfully acquired and quantified, unlike in our early study,<sup>7</sup> in which only XRF images of the right kidney were available to quantify GNP concentrations. Therefore, in the present study, the GNP clearance data (i.e., excretion rate) for both kidneys were much more comparable with the results of previous studies.<sup>25,26</sup> Furthermore, compared to our early study,<sup>7</sup> the radiation dose delivered to the mice for XRF image acquisition was reduced by about half (107 to 59.1 mGy), and the detection limit was improved ( $\sim 0.125$  to  $\sim 0.07$  wt%). This was because the change of the horizontal bed geometry reduced Compton-backscattered photons that caused noise in the XRF images and unnecessary radiation dose.

CT images of mice were acquired using FPD and were fused with the XRF images. The CT image resolution (i.e., 6.2 LP/cm at 50% MTF) was comparable to that reported by the benchtop XFCT and CT system using the same FPD.<sup>24</sup> With additional anatomic images, the CT/XRF fusion images confirmed the validity of the functional information provided by the XRF image. In a typical small animal in vivo micro-CT, the imaged object is stationary and a rotating gantry geometry, in which the X-ray tube and detector rotate, is the most common.<sup>27</sup> However, the X-ray tube and detector of the current system were stationary, whereas the mouse was rotated horizontally. Therefore, in the current CT acquisition setup, the mouse was kept upside-down during part of the CT scan, and as a result, motion artifacts due to gravity appeared on CT images. However, we postulated that the horizontal rotation of the mouse and motion artifacts were acceptable in terms of animal well-being and practical application. This is because there were no other devices suffering the mouse, and motion artifacts appeared mostly on the surface of the mouse. Nevertheless, it is still necessary to develop a horizontal bed to minimize motion artifacts by reducing the movement of soft tissues.

The radiation dose (321.7 mGy) delivered to the mice for CT image acquisition was comparable with that suggested by micro-CT studies.<sup>28,29</sup> Nevertheless, we should reduce radiation dose by optimizing tube voltage, tube current, filter material, and scanning procedure. Increasing the tube voltage can accomplish better photon counting statistics, less noise, and less radiation dose with a shorter scan time. Considering the exposure time (47 ms) of the FPD, the radiation dose can be reduced by decreasing the scan time per projection (3 s)

for CT image acquisition. Furthermore, the use of MNPs with relatively low K-edge energies, such as europium (i.e., 48.5 keV) and gadolinium (i.e., 50.2 keV), can simultaneously acquire XRF and CT images using a single X-ray spectrum. Thus, the radiation dose for acquiring CT/XRF fusion images can be further reduced.

GNPs having 1.9 nm-diameter and no surface modification were injected into tumor-bearing mice. Therefore, GNPs can be leaked and accumulated into the tumor interstitium through the tumor vasculature by relying mainly on the enhanced permeability and retention effect (i.e., passive targeting).<sup>30</sup> However, many studies have shown that therapeutic particles that were smaller than 10 nm extravasated to normal tissues.<sup>31–33</sup> In addition, most of the GNPs for the in vivo studies went through nonspecific opsonization adsorbed opsonin to the GNPs and were removed by the reticuloendothelial system for the immune response.<sup>34</sup> As expected, the GNP concentration of the tumor was much lower than that of the liver or spleen. It may be inappropriate to expect tumor accumulation of 1.9 nm GNPs by only relying on a passive targeting strategy without any surface modifications. In order to improve tumor targeting ability, various ligands, such as antibodies for active targeting<sup>35</sup> and polyethylene glycol for passive targeting,<sup>36</sup> can be modified on the surface of GNPs to enhance tumor accumulation.

The GNP concentrations in the kidneys measured by the pinhole XRF imaging system were comparable to those by the L-shell XRF detection system and ICP-MS, with a difference of 0.01–0.08 wt%. In our early study,<sup>7</sup> an excision of the extracted kidneys for ex vivo measurements was a major cause of the discrepancies between in vivo and ex vivo GNP concentrations (0.19–0.23 wt%). On the other hand, in the present study, the kidneys were not excised and were measured by the L-shell XRF detection system and ICP-MS. The L-shell XRF detection system was successfully validated and confirmed by ICP-MS and the pinhole XRF imaging system. It will be a promising modality for ex vivo quantification of GNP concentrations with in situ convenience and superior detection limit. The ex vivo quantification limit of GNP concentration using this system was about 10 times lower than in our early study ( $\sim 0.02$  wt% vs.  $\sim 0.2$  wt%).

Nevertheless, some technical challenges in the L-shell XRF detection system need further improvement. First, a collimator is required to reduce unwanted photons that can cause noise in the L-shell XRF photon counts and interfere with the precise measurement of GNP concentrations. Second, one should correct the self-absorption of L-shell XRF photon counts and obtain a linear relationship between GNP concentrations and the corrected L-shell XRF photon counts. In this study, the self-absorption of L-shell XRF photons was not explicitly taken into account because it was negligible in the GNP concentrations of the extracted

organs (up to 0.12 wt%). However, in order to ensure the validity of the L-shell XRF detection system, a self-absorption correction of L-shell XRF photons needs to be more quantitatively addressed in the future. Third, organ samples prepared through a homogenization process that renders lyophilized and dissolved forms should be used to minimize the uncertainty brought about by the heterogeneous distribution of GNPs in the organs.

The current pinhole XRF imaging system can acquire XRF images within 2 min, but the detection limit needs to be improved to at least 0.01 wt%. In order to overcome the limitations of the direct subtraction method, the 2D convolutional neural network (CNN) model for Compton background elimination can be used to acquire XRF images without preinjection scanning.<sup>37</sup> Therefore, the image acquisition time and radiation dose can be reduced by half while maintaining the quality of XRF images. Alternatively, by doubling the postinjection scanning time, more XRF photon counts can be obtained while maintaining the image acquisition time and radiation dose, and the detection limit can be improved. In particular, acquiring XRF images without preinjection scanning means no need to restrain mice under anesthesia during XRF imaging. This allows to wake up and leave free the mice between anesthesia sessions, and thus, mice can be scanned repeatedly at any time after an injection of GNP-containing solution. However, the 2D CNN model at the current training stage has difficulty in acquiring reliable *in vivo* XRF images due to a lack of training datasets. In addition, there is a need to seek a new filter material that can improve the quality of XRF images and the detection limit. The detection limit can be further improved by replacing a commercial CZT pixelated detector with a commercial cadmium telluride (CdTe) pixelated detector, which has a better energy resolution and a higher maximum count rate.<sup>38</sup> However, due to the small size of the CdTe pixelated detector FOV (i.e., 2 cm × 2 cm), it is currently might not be suitable for preclinical studies on small animals.

## 5 | CONCLUSIONS

A dual imaging modality of pinhole XRF and CT system with a 2D CZT gamma camera and FPD was successfully developed. The XRF and CT images of living mice were acquired and fused to provide time-lapse functional and anatomic information. In particular, time-lapse XRF images in the organs provided valuable insight into the pharmacokinetics of 1.9 nm bare GNPs. The *in vivo* and *ex vivo* biodistributions of GNPs measured by pinhole XRF images and L-shell XRF detection, respectively, were validated by ICP-MS. The procedure of the L-shell XRF detection system to measure MNP concentrations was easier than that of ICP-MS. Once the aforementioned technical challenges are addressed, a dual imaging modality of pinhole XRF and CT sys-

tem together with L-shell XRF detection system can be routine *in vivo* imaging and *ex vivo* quantification for preclinical studies using MNPs.

## ACKNOWLEDGMENTS


This work was supported by the Korea government (MSIT) (1711078081) and the Nuclear Safety Research Program through the Korea Foundation Of Nuclear Safety (KoFONS) using the financial resource granted by the Nuclear Safety and Security Commission (NSSC) of the Republic of Korea (No. 2003021).

## CONFLICTS OF INTEREST


The authors have no conflicts to disclose.

## ORCID

Taeyun Kim  <https://orcid.org/0000-0003-2846-140X>

Seongmoon Jung 

<https://orcid.org/0000-0002-9483-158X>

Hyung-Jun Im 

<https://orcid.org/0000-0002-4368-6685>

Sung-Joon Ye 

<https://orcid.org/0000-0001-8714-6317>

## REFERENCES

1. Kwatra D, Venugopal A, Anant S. Nanoparticles in radiation therapy: a summary of various approaches to enhance radiosensitization in cancer. *Transl Cancer Res*. 2013;2(4):330-342.
2. Hainfeld JF, Slatkin DN, Smilowitz HM. The use of gold nanoparticles to enhance radiotherapy in mice. *Phys Med Biol*. 2004;49(18):N309-N315.
3. Cho SH, Krishnan S. *Cancer Nanotechnology: Principles and Applications in Radiation Oncology*. CRC Press; 2013.
4. Schuemann J, Berbeco R, Chithrani DB, et al. Roadmap to clinical use of gold nanoparticles for radiation sensitization. *Int J Radiat Oncol Biol Phys*. 2016;94(1):189-205.
5. Her S, Jaffray DA, Allen C. Gold nanoparticles for applications in cancer radiotherapy: mechanisms and recent advancements. *Adv Drug Deliv Rev*. 2017;109:84-101.
6. Singh P, Pandit S, Mokkapati V, Garg A, Ravikumar V, Mijakovic I. Gold nanoparticles in diagnostics and therapeutics for human cancer. *Int J Mol Sci*. 2018;19(7):1979.
7. Jung S, Kim T, Lee W, et al. Dynamic *in vivo* x-ray fluorescence imaging of gold in living mice exposed to gold nanoparticles. *IEEE Trans Med Imaging*. 2020;39(2):526-533.
8. Larsson JC, Vogt C, Vagberg W, et al. High-spatial-resolution x-ray fluorescence tomography with spectrally matched nanoparticles. *Phys Med Biol*. 2018;63(16):164001.
9. Li W, Chen X. Gold nanoparticles for photoacoustic imaging. *Nanomedicine*. 2015;10(2):299-320.
10. Siddique S, Chow JCL. Application of nanomaterials in biomedical imaging and cancer therapy. *Nanomaterials (Basel)*. 2020;10(9):1700.
11. James ML, Gambhir SS. A molecular imaging primer: modalities, imaging agents, and applications. *Physiol Rev*. 2012;92(2):897-965.
12. Cheong SK, Jones BL, Siddiqi AK, Liu F, Manohar N, Cho SH. X-ray fluorescence computed tomography (XFCT) imaging of gold nanoparticle-loaded objects using 110 kVp x-rays. *Phys Med Biol*. 2010;55(3):647-662.
13. Manohar N, Reynoso FJ, Cho SH. Experimental demonstration of direct L-shell x-ray fluorescence imaging of gold nanoparticles using a benchtop x-ray source. *Med Phys*. 2013;40(8):080702.

14. Manohar N, Jones BL, Cho SH. Improving x-ray fluorescence signal for benchtop polychromatic cone-beam x-ray fluorescence computed tomography by incident x-ray spectrum optimization: a Monte Carlo study. *Med Phys*. 2014;41(10):101906.
15. Jung S, Sung W, Ye SJ. Pinhole x-ray fluorescence imaging of gadolinium and gold nanoparticles using polychromatic x-rays: a Monte Carlo study. *Int J Nanomedicine*. 2017;12:5805-5817.
16. Manohar N, Reynoso FJ, Diagaradjane P, Krishnan S, Cho SH. Quantitative imaging of gold nanoparticle distribution in a tumor-bearing mouse using benchtop x-ray fluorescence computed tomography. *Sci Rep*. 2016;6:22079.
17. Townsend DW. Dual-modality imaging: combining anatomy and function. *J Nucl Med*. 2008;49(6):938-955.
18. Zhang W, Zhang S, Gao P, et al. The feasibility of NaGdF<sub>4</sub> nanoparticles as an x-ray fluorescence computed tomography imaging probe for the liver and lungs. *Med Phys*. 2020;47(2):662-671.
19. Shaker K, Vogt C, Katsu-Jimenez Y, et al. Longitudinal in vivo x-ray fluorescence computed tomography with molybdenum nanoparticles. *IEEE Trans Med Imaging*. 2020;39(12):3910-3919.
20. Saladino GM, Vogt C, Li Y, et al. Optical and x-ray fluorescent nanoparticles for dual mode bioimaging. *ACS Nano*. 2021;15(3):5077-5085.
21. Cherry SR, Sorenson JA, Phelps ME. *Physics in Nuclear Medicine e-Book*. Elsevier Health Sciences; 2012.
22. Eldib ME, Hegazy M, Mun YJ, Cho MH, Cho MH, Lee SY. A ring artifact correction method: validation by micro-CT imaging with flat-panel detectors and a 2D photon-counting detector. *Sensors (Basel)*. 2017;17(2):269.
23. Anam C, Fujibuchi T, Budi WS, Haryanto F, Dougherty G. An algorithm for automated modulation transfer function measurement using an edge of a PMMA phantom: impact of field of view on spatial resolution of CT images. *J Appl Clin Med*. 2018;19(6):244-252.
24. Deng L, Yasar S, Ahmed MF, et al. Investigation of transmission computed tomography (CT) image quality and x-ray dose achievable from an experimental dual-mode benchtop x-ray fluorescence CT and transmission CT system. *J X-Ray Sci Technol*. 2019;27(3):431-442.
25. Hainfeld JF, Slatkin DN, Focella TM, Smilowitz HM. Gold nanoparticles: a new x-ray contrast agent. *Br J Radiol*. 2006;79(939):248-253.
26. Xu J, Yu M, Carter P, et al. In vivo x-ray imaging of transport of renal clearable gold nanoparticles in the kidneys. *Angew Chem Int Ed Engl*. 2017;56(43):13356-13360.
27. Clark DP, Badea CT. Micro-CT of rodents: state-of-the-art and future perspectives. *Phys Med*. 2014;30(6):619-634.
28. Berghen N, Dekoster K, Marien E, et al. Radiosafe micro-computed tomography for longitudinal evaluation of murine disease models. *Sci Rep*. 2019;9:17598.
29. Rueda AN, Ruiz-Trejo C, López-Pineda E, Romero-Piña ME, Medina LA. Dosimetric evaluation in micro-CT studies used in preclinical molecular imaging. *Appl Sci*. 2021;11(17):7930.
30. Sun T, Zhang YS, Pang B, Hyun DC, Yang M, Xia Y. Engineered nanoparticles for drug delivery in cancer therapy. *Angew Chem Int Ed Engl*. 2014;53(46):12320-12364.
31. Stylianopoulos T. EPR-effect: utilizing size-dependent nanoparticle delivery to solid tumors. *Ther Deliv*. 2013;4(4):421-423.
32. Sarin H. Physiologic upper limits of pore size of different blood capillary types and another perspective on the dual pore theory of microvascular permeability. *J Angiogenesis Res*. 2010;2(1):1-19.
33. Hobbs SK, Monsky WL, Yuan F, et al. Regulation of transport pathways in tumor vessels: role of tumor type and microenvironment. *Proc Natl Acad Sci USA*. 1998;95(8):4607-4612.
34. Nie S. Understanding and overcoming major barriers in cancer nanomedicine. *Nanomedicine (Lond)*. 2010;5(4):523-528.
35. El-Sayed IH, Huang X, El-Sayed MA. Surface plasmon resonance scattering and absorption of anti-EGFR antibody conjugated gold nanoparticles in cancer diagnostics: applications in oral cancer. *Nano Lett*. 2005;5(5):829-834.
36. Peracchia M, Fattal E, Desmaele D, et al. Stealth® PEGylated polycyanoacrylate nanoparticles for intravenous administration and splenic targeting. *J Control Release*. 1999;60(1):121-128.
37. Jung S, Lee J, Cho H, Kim T, Ye S-J. Compton background elimination for in vivo x-ray fluorescence imaging of gold nanoparticles using convolutional neural network. *IEEE Trans Nucl Sci*. 2020;67(11):2311-2320.
38. Jayarathna S, Ahmed MF, O'ryan L, Moktan H, Cui Y, Cho SH. Characterization of a pixelated cadmium telluride detector system using a polychromatic x-ray source and gold nanoparticle-loaded phantoms for benchtop x-ray fluorescence imaging. *IEEE Access*. 2021;9:49912-49919.

**How to cite this article:** Kim T, Lee WS, Jeon M, et al. Dual imaging modality of fluorescence and transmission X-rays for gold nanoparticle-injected living mice. *Med Phys*. 2023;50:529–539.  
<https://doi.org/10.1002/mp.16070>